



Characteristics of Fe and Mn bearing precipitates generated by Fe(II) and Mn(II) co-oxidation with O₂, MnO₄ and HOCl in the presence of groundwater ions

Arslan Ahmad^{a, b, c, d, *}, Albert van der Wal^{c, d}, Prosun Bhattacharya^{b, e},
Case M. van Genuchten^{f, g, **}

^a KWR Water Cycle Research Institute, Nieuwegein, the Netherlands

^b KTH-International Groundwater Arsenic Research Group, Department of Sustainable Development, Environmental Science and Engineering, KTH Royal Institute of Technology, Stockholm, Sweden

^c Department of Environmental Technology, Wageningen University and Research (WUR), Wageningen, the Netherlands

^d Evides Water Company, N.V. Rotterdam, the Netherlands

^e International Centre for Applied Climate Science, University of Southern Queensland, Toowoomba, Australia

^f Geochemical Department, Geological Survey of Denmark and Greenland (GEUS), Copenhagen, Denmark

^g Department of Earth Sciences-Geochemistry, Faculty of Geosciences, Utrecht University, Utrecht, the Netherlands

ARTICLE INFO

Article history:

Received 5 April 2019

Received in revised form

6 June 2019

Accepted 13 June 2019

Available online 14 June 2019

Keywords:

Mn and Fe removal

Drinking water

Filtration

Iron and manganese oxidation and precipitation

Groundwater treatment

X-ray absorption spectroscopy

ABSTRACT

In this work, we combined macroscopic measurements of precipitate aggregation and chemical composition (Mn/Fe solids ratio) with Fe and Mn K-edge X-ray absorption spectroscopy to investigate the solids formed by co-oxidation of Fe(II) and Mn(II) with O₂, MnO₄, and HOCl in the presence of groundwater ions. In the absence of the strongly sorbing oxyanions, phosphate (P) and silicate (Si), and calcium (Ca), O₂ and HOCl produced suspensions that aggregated rapidly, whereas co-oxidation of Fe(II) and Mn(II) by MnO₄ generated colloidal stable suspensions. The aggregation of all suspensions decreased in P and Si solutions, but Ca counteracted these oxyanion effects. The speciation of oxidized Fe and Mn in the absence of P and Si also depended on the oxidant, with O₂ producing Mn(III)-incorporated lepidocrocite (Mn/Fe = 0.01–0.02 mol/mol), HOCl producing Mn(III)-incorporated hydrous ferric oxide (HFO) (Mn/Fe = 0.08 mol/mol), and MnO₄ producing poorly-ordered MnO₂ and HFO (Mn/Fe > 0.5 mol/mol). In general, the presence of P and Si decreased the crystallinity of the Fe(III) phase and increased the Mn/Fe solids ratio, which was found by Mn K-edge XAS analysis to be due to an increase in surface-bound Mn(II). By contrast, Ca decreased the Mn/Fe solids ratio and decreased the fraction of Mn(II) associated with the solids, suggesting that Ca and Mn(II) compete for sorption sites. Based on these results, we discuss strategies to optimize the design (i.e. filter bed operation and chemical dosing) of water treatment plants that aim to remove Fe(II) and Mn(II) by co-oxidation.

© 2019 The Authors. Published by Elsevier Ltd. This is an open access article under the CC BY license (<http://creativecommons.org/licenses/by/4.0/>).

1. Introduction

Groundwater is treated to remove dissolved iron (Fe(II)) and manganese (Mn(II)) to avoid sedimentation in distribution pipelines and discoloration of treated water (Vries et al., 2017). Typical

schemes at groundwater treatment plants consist of aeration followed by rapid sand filtration (de Moel et al., 2006). Aeration saturates the groundwater with dissolved oxygen (O₂), which facilitates oxidation and precipitation of Fe and Mn solids. The Fe and Mn bearing precipitates accumulate in filters until backwashing is applied to dislodge the solids from the filtration media. While O₂ is often capable of oxidizing Fe(II) on the time scale of typical groundwater treatment, O₂ alone is ineffective at oxidizing Mn(II) to Mn(III,IV) and As(III) to As(V), the more easily removed arsenic species (Diem and Stumm, 1984; Gude et al., 2016; Van Beek et al., 2012). To rapidly oxidize Mn(II) and As(III) at water treatment plants, stronger chemical oxidants, such as NaOCl or KMnO₄, can be

* Corresponding author. KWR Water Cycle Research Institute, Nieuwegein, the Netherlands.

** Corresponding author. Geological Survey of Denmark and Greenland (GEUS), Copenhagen, Denmark.

E-mail addresses: arslan.ahmad@kwrwater.nl (A. Ahmad), cvg@geus.dk (C.M. van Genuchten).

used (Ahmad et al., 2018; Sorlini and Gialdini, 2010). Strong oxidants are also used when high concentrations of Fe(II) are present in groundwater and rapid oxidation is desired (Allard et al., 2013; Knocke et al., 1991).

Although chemical oxidants (i.e. NaOCl and KMnO_4) can improve co-oxidative removal of Fe(II), Mn(II) and As(III), little is known about how different oxidants impact key properties of the solid end-products, including the structure and composition. Previous work has shown that the Fe(II) and Mn(II) oxidation rates alter the structure of the solid phase. For example, poorly-ordered Fe(III) precipitates result from rapid Fe(II) oxidation by H_2O_2 and moderately crystalline lepidocrocite forms from slower Fe(II) oxidation by O_2 (van Genuchten and Pena, 2017; Voegelin et al., 2010). These differences in crystallinity are important because poorly-ordered Fe(III) (oxyhydr)oxides have a higher specific surface area than crystalline solids, which would increase sorption of ions (e.g. As) per mass of Fe added. Similarly, poorly-ordered Mn(IV) oxides are favoured when microorganisms oxidize Mn(II) rapidly, whereas Mn(III) oxides can form from slow, surface-catalyzed Mn(II) oxidation by O_2 (Lan et al., 2017; Tebo et al., 2005). However, the co-occurrence of Fe(II) and Mn(II), which is common in groundwater (McArthur et al., 2012), can alter the pathways of co-oxidation since strong Fenton-type oxidants generated from Fe(II) oxidation can react rapidly with reduced species, including Mn(II) (Hug and Leupin, 2003; van Genuchten and Pena, 2017). In addition to the type of chemical oxidant, the structure of Fe and Mn bearing solids can also be altered by the presence of common groundwater ions, such as silicate (Si), phosphate (P), As, and calcium (Ca). By binding strongly to precipitate surfaces, P and Si oxyanions can inhibit crystal growth, leading to poorly-ordered solids (Kaegi et al., 2010; Senn et al., 2017). Moreover, Si and P oxyanions can decrease the particle surface charge, which strongly influences particle aggregation and sedimentation efficiency (Sposito, 2008), whereas Ca can counteract the effects of P and Si. Since the sorption reactivity and colloidal stability of Fe and Mn precipitates depend strongly on their structure and composition, it is critical to investigate how structural properties of the precipitates are altered by oxidant type and solution composition.

In this work, we combine macroscopic measurements of aggregation and sedimentation (i.e. turbidity and filterability) with Fe

and Mn K-edge X-ray absorption spectroscopy to investigate the solids formed by Fe(II) and Mn(II) co-oxidation with O_2 , MnO_4 , and HOCl. We perform batch Fe(II) and Mn(II) co-oxidation experiments in solutions with systematically varied concentrations of As, P, Si, and Ca. We focus primarily on characterizing the speciation of Fe and Mn in this work, but note that the redox and sorption behavior of As in identical experiments will be reported in a follow-up study. The knowledge generated in our investigation is critical to select the most effective oxidant in groundwater treatment, considering the co-removal of Fe(II), Mn(II) and As(III) and the aggregation properties of the end-products.

2. Materials and methods

2.1. Chemicals

All chemicals were reagent grade. The stock solutions for Fe(II), Mn(II) and HOCl were prepared by dissolving 24.9 g/l $\text{FeSO}_4 \cdot 7\text{H}_2\text{O}$ (Boom BV[®]), 1.8 g/l MnCl_2 (Merck[®]) and 4.66 g/l NaOCl (Acors Organics[®]) in 100 mL oxygen-free ultrapure water (18.2 M Ω cm, Purelab[®] Chorus: Veolia Water). The stock solutions for Si, HCO_3 , NaCl and MnO_4 were prepared by dissolving 75.7 g/l $\text{Na}_2\text{SiO}_3 \cdot 5\text{H}_2\text{O}$ (Aldrich[®]), 0.87 g/l NaHCO_3 (J.T. Baker[®]), 0.26 g/l NaCl (J.T. Baker[®]) and 6.3 g/l KMnO_4 (J.T. Baker[®]) in ultrapure water. The stock solutions for P and Ca were obtained by dissolving 1.11 g/l $\text{NaH}_2\text{PO}_4 \cdot \text{H}_2\text{O}$ (J.T. Baker[®]) and 138.5 g/l CaCl_2 (J.T. Baker[®]) in 0.1 M HCl. For As(III) addition, a certified solution (1000 mg As(III)/L, Inorganic Ventures[®]) set in HCl matrix was used without any dilution. For pH control during the experiments, 0.1 M NaOH and 0.1 M HCl solutions were used.

2.2. Oxidation and precipitation experiments

Experiments were performed with a 5 L glass reactor connected to a controller (ez-Control, Applikon[®] Biotechnology) for adjusting, maintaining and logging (BioXpertV2 software) reaction parameters, including the pH, temperature, oxidant supply and stirring speed (Fig. 1). The experiments were carried out at pH 7.5 and 20 °C, with stirring set to 100 rpm. Fe(II) and Mn(II) oxidation was initiated by dosing O_2 , KMnO_4 or NaOCl to anaerobic solutions that initially contained Fe(II), Mn(II), As(III), Si, P and Ca in different

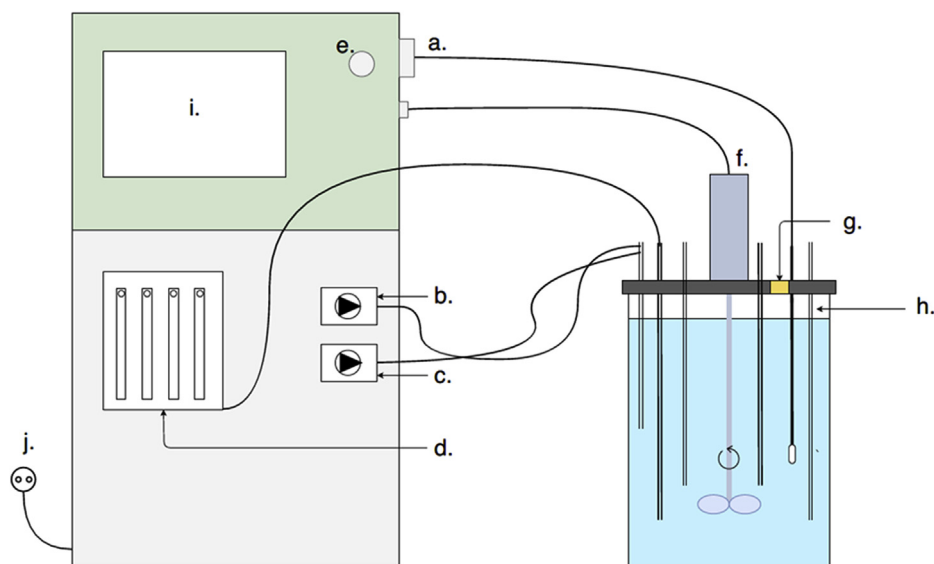


Fig. 1. A schematic overview of the assembly used in precipitation and settling experiments. a. data logger (pH, temperature, dissolved oxygen); b. acid pump; c. alkali pump; d. nitrogen and air supply; e. on/off; f. stirrer; g. chemical injection port; h. sampling port; i. controller display; j. power supply.

Table 1
Nomenclature, initial composition, Fe and Mn removed by 0.45 μm filtration and solids ratio in O_2 , MnO_4 and HOCl experiments.

Experiment code	Initial solution composition											Fe and Mn removed by 0.45 μm filter						Solids ratio		
												O_2		MnO_4		HOCl		O_2	MnO_4	HOCl
	Fe	Mn	As	Si	P	Ca	Mn/Fe	As/Fe	Si/Fe	P/Fe	Ca/Fe	Fe	Mn	Fe	Mn	Fe	Mn	Mn/Fe	Mn/Fe	Mn/Fe
	($\mu\text{mol/L}$)						(molar ratio)					(%)	(%)	(%)	(%)	(%)	(%)	(molar ratio)	(molar ratio)	(molar ratio)
Ref	90	9	0.7	–	–	–	0.1	0.008	–	–	–	99.9	18.6	54.5	44.8	99.1	79.6	0.01	0.50	0.08
Mn18	90	18	0.7	–	–	–	0.2	0.008	–	–	–	99.9	8.2	6.1	55.6	98.3	83.2	0.02	x	0.18
Si150	90	9	0.7	150	–	–	0.1	0.008	1.7	–	–	67.4	16.0	27.0	23.0	80.7	57.4	0.03	0.53	0.08
Si350	90	9	0.7	350	–	–	0.1	0.008	3.9	–	–	2.2	5.8	*	*	35.4	28.6	x	*	0.08
Si750	90	9	0.7	750	–	–	0.1	0.008	8.3	–	–	0.0	1.9	4.8	16.6	12.0	12.0	x	x	x
Si350 + Ca500	90	9	0.7	350	–	500	0.1	0.008	3.9	–	6	96.8	26.0	99.8	93.2	97.7	47.2	0.03	0.53	0.05
Si750 + Ca1000	90	9	0.7	750	–	1000	0.1	0.008	8.3	–	11	95.7	16.8	99.8	92.4	95.8	45.9	0.02	0.56	0.05
Si750 + Ca2500	90	9	0.7	750	–	2500	0.1	0.008	8.3	–	28	92.1	13.0	99.9	93.0	97.7	50.5	0.01	0.56	0.06
P4	90	9	0.7	–	4	–	0.1	0.008	–	0.04	–	98.9	30.0	34.7	24.1	98.4	75.1	0.03	0.52	0.08
P10	90	9	0.7	–	10	–	0.1	0.008	–	0.11	–	96.8	36.7	9.3	9.8	96.5	68.0	0.04	x	0.08
P16	90	9	0.7	–	16	–	0.1	0.008	–	0.18	–	89.0	39.0	0.0	4.4	75.1	51.4	0.05	x	0.08
P16 + Ca1000	90	9	0.7	–	16	1000	0.1	0.008	–	0.18	11	99.9	14.8	99.9	87.2	99.9	50.0	0.02	0.54	0.05

* Data not available.

x Not determined because of low precipitate retention.

The (range of) concentration of Fe, Mn, As, Si, P and Ca in the initial solution in mg/L was 5.0, 0.5, 0.05, 5.0–20, 0.1–0.5 and 20–100, respectively.

concentrations (Table 1). We note that NaOCl addition results in approximately 50% HOCl and 50% OCl^- at pH 7.5 ($\text{pK}_{\text{aHOCl}} = 7.5$). The range of ionic compositions studied in this work was derived from an analysis of groundwater quality in the Netherlands (Ahmad et al., 2015). For each oxidant, the initial solutions in the reference experiments (herein referred to as Ref) contained 90 μM Fe(II) (5.0 mg/L), 9.0 μM Mn(II) (0.5 mg/L) and 0.7 μM As(III) (0.05 mg/L) without Si, P and Ca. In Mn18 experiments, the initial solution contained 18 μM Mn instead of 9 μM Mn. The rest of the experiments are identified by the ions added in μM to the Ref solution (i.e. Si150 consists of 150 μM Si, 90 μM Fe(II), 9.0 μM Mn(II) and 0.7 μM As(III)). All solutions also contained 2.5 mM NaHCO_3 and 0.6 mM NaCl to provide alkalinity and ionic strength.

For the O_2 experiments, the initial solutions were bubbled with air to reach saturation (≈ 9 mg O_2/L). For MnO_4 and HOCl systems, the doses of the KMnO_4 and NaOCl stocks were based on the combined stoichiometric demand of Fe(II), Mn(II) and As(III) oxidation to produce Fe(III), Mn(IV) and As(V), respectively (chemical reactions are provided in the Supplementary Data) (Ghurye and Clifford, 2001).

The experimental procedure included: (i) preparation of the initial solutions in the reaction vessel under anaerobic conditions, (ii) dosing the oxidant (O_2 , MnO_4 or HOCl) and allowing for oxidation and precipitation while stirring at 100 rpm and (iii) collection of suspension samples 30 min after oxidant addition, which were filtered over 0.45 μm filters and stored for subsequent analysis. A 30 min reaction interval was selected based on PHREEQC simulations showing complete Fe(II) oxidation in the O_2 system in 30 min (Fig. S1). Samples for aqueous and total Fe and Mn were collected in 100 mL plastic bottles that contained 0.5 mL of 65% HNO_3 and were stored at 4 $^\circ\text{C}$ until analysis by Inductively Coupled Plasma Mass Spectrometry (ICP-MS) (Thermo Scientific XSERIES 2 ICP-MS, Thermo Fisher Scientific, Breda, The Netherlands) at Aqualab Zuid B.V. in The Netherlands. The removal of Mn and Fe and the Mn/Fe solid ratios (mol/mol) were determined from the difference between the Fe and Mn concentrations of the initial and final filtered solutions. Solids generated in each experiment were also collected and reserved for XAS analysis.

2.3. Settling experiments

The aggregation and settling characteristics of the particles were studied by measuring the turbidity of the suspensions as a function

of time using a 2100Q Portable Turbidimeter, Hach[®] USA. Following the addition of oxidant and 30 min of mixing, the initial turbidity of the suspension was measured by removing an aliquot 5 cm below the water surface during mixing. After the initial turbidity measurement, the stirring was stopped and the suspension was allowed to settle by gravity. A second turbidity measurement was made after 1 h of settling by removing another aliquot 5 cm below the water surface. The turbidity measurement vessel was rinsed twice with ultrapure water and oxalic acid (pH 1–3) between measurements.

2.4. X-ray absorption spectroscopy

2.4.1. Data collection

X-ray absorption spectra at the Fe and Mn K-edges were collected at room temperature at beamline 4–1 of the Stanford Synchrotron Radiation Lightsource (SSRL) and the DUBBLE beamline (BM-26a) of the European Synchrotron Radiation Facility (ESRF). The design of the DUBBLE beamline is described by Borsboom et al. (1998) and Nikitenko et al. (2008). Fe K-edge XAS data were recorded in transmission mode out to k of 13 \AA^{-1} . Mn K-edge XAS data were collected in transmission and fluorescence modes out to k of 12 \AA^{-1} , with spectra of superior data quality selected for subsequent analysis. Fe (0) or Mn (0) foils were used to calibrate the beam at 7112 eV or 6539 eV, respectively. Spectra were aligned, averaged and background-subtracted using SixPack software (Webb, 2005) following standard methods described previously (van Genuchten et al., 2012). The k^3 -weighted EXAFS spectra ($\chi(k)k^3$) were Fourier-transformed using a Kaiser-Bessel window with dk of 3 \AA^{-1} typically over the k -range 2–12 \AA^{-1} for the Fe spectra and 2–10.5 \AA^{-1} for the Mn spectra. Further details of the data collection are given in the Supplementary Data.

2.4.2. Data analysis

The Fe K-edge EXAFS spectra were analyzed by principal component analysis (PCA) and linear combination fits (LCFs). For the PCA, the ITFA program suite (Rossberg et al., 2003; Scheinost et al., 2006) was used to determine the number of independent components that reproduced the major variance of the data set based on minimizing the indicator (IND) function. The LCFs were performed with the SixPack software (Webb, 2005) using the EXAFS spectra of Fe(III)-bearing standard minerals. Details on the synthesis of these standards (e.g. lepidocrocite, 2-line ferrihydrite,

oxyanion-rich hydrous ferric oxide) are reported elsewhere (van Genuchten et al., 2018; van Genuchten et al., 2014a). The fit-derived fractions of the standards in each sample were normalized to one.

The Mn K-edge XANES spectra were analyzed by LCFs to determine the fraction of solid-associated Mn(II), Mn(III), and Mn(IV). SixPack software was used to perform the LCFs on the normalized XANES spectra, with a fit range of 6530–6590 eV. The Mn K-edge EXAFS spectra of representative samples were analyzed by shell-by-shell fits. Since the presence of multiple Mn oxidation states in a single sample complicates the interpretation of shell-by-shell fits, we applied this approach on samples that were determined by XANES LCFs to consist of primarily a single oxidation state (i.e. Mn(II), Mn(III), or Mn(IV)). Theoretical curve fits were performed in $R + \Delta R$ -space (Å) using the SixPack software with algorithms based on the IFEFFIT library (Newville, 2001). Single scattering paths (Mn–O, Mn–Mn) were derived from the structure of birnessite (MnO₂) (Lanson et al., 2002), with theoretical phase and amplitude functions calculated using FEFF6 (Rehr et al., 1992). Because Mn and Fe have similar atomic numbers, these backscattering atoms cannot be distinguished in shell-by-shell fits. Consequently, the second shell fitting results for the Mn data are reported as $CN_{Mn-Mn/Fe}$ and $R_{Mn-Mn/Fe}$. The goodness-of-fit was assessed based on the R-factor, which is the mean square difference between the fit and the data on a point-by-point basis: $R = \frac{\sum_i (data_i - fit_i)^2}{\sum_i (data_i)^2}$. A reasonable fit is considered to yield an R-factor less than 0.05 (Kelly et al., 2008). A similar shell-by-shell fitting approach was followed for select Fe spectra. Further details regarding the XANES and EXAFS analyses are reporting in the Supplementary Data.

3. Results

3.1. Macroscopic precipitate properties

3.1.1. Settling and filterability

In the O₂ system, the Ref and Mn18 experiments had an initial turbidity of ≈ 8 NTU (Fig. 2) and a similarly low final turbidity of < 3 NTU ($\approx 70\%$ turbidity decrease), which indicates rapid flocculation and sedimentation. These particles were highly filterable ($> 99\%$) by 0.45 μm filters (pore size used to approximate filterable particles in rapid sand filters). The addition of 150–750 μM Si decreased the initial turbidity from 6 to 2 NTU, resulting in translucent light yellow suspensions that were colloidally stable (i.e. no difference in initial and final turbidity, Fig. 2A, and low filterability, Table 1). The addition of Ca to the 350 and 750 μM Si solutions increased the initial turbidity to match the Ref O₂ sample, but the final turbidity was higher than the Ref O₂ sample. In the P series, 4 and 10 μM P did not alter significantly the initial or final turbidity relative to the Ref O₂ sample and the precipitates settled effectively ($\approx 65\%$ turbidity decrease). However, the 16 μM P experiment resulted in a colloidally stable suspension. When 1000 μM Ca was added to the 16 μM P solution, the suspension had the highest initial turbidity in the O₂ experiments (14 NTU), with effective turbidity reduction (70%) and good filterability ($> 99\%$ Fe removed, Table 1).

The settling behavior and filterability of the precipitates formed in the MnO₄ system (Fig. 2B, Table 1) differed considerably from those in the O₂ system. The darker Ref and Mn18 suspensions formed in the MnO₄ system were colloidally stable, having initial and final turbidity > 5.5 NTU, which contrasts the rapid settling of the Ref O₂ sample. The 150–750 μM Si samples in the MnO₄ system were also colloidally stable, but the initial turbidity was slightly lower than the Ref MnO₄ sample. The addition of Ca to the Si solutions produced cloudy suspensions that settled more effectively ($\approx 60\%$ turbidity decrease) than the Ca + Si samples in the O₂

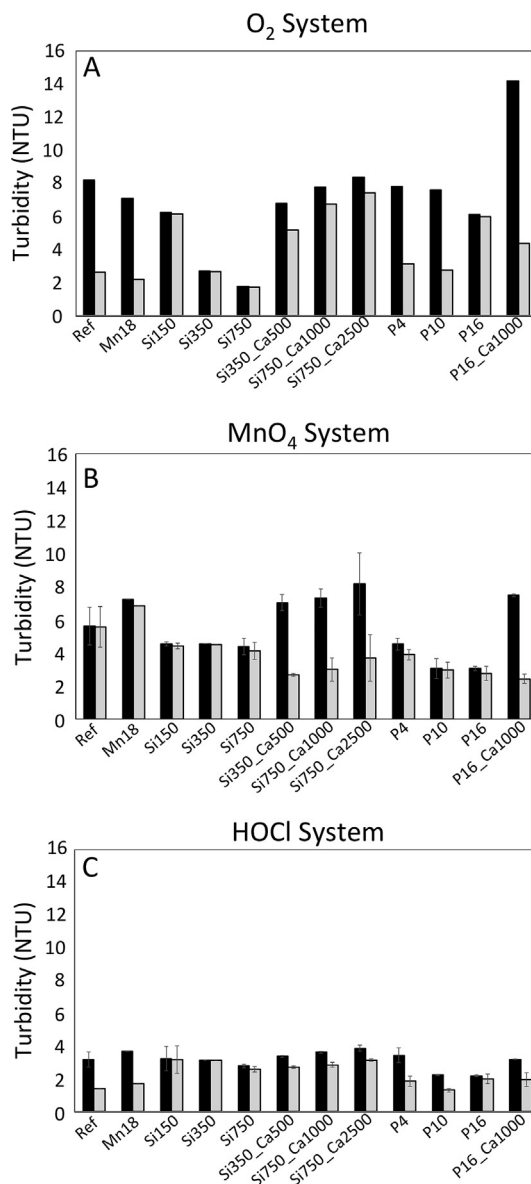


Fig. 2. Initial and final turbidity as function of the oxidant used and solution composition. A. O₂ system, B. MnO₄ system, C. HOCl system.

system. The 4, 10 and 16 μM P samples in the MnO₄ system were all colloidally stable (turbidity = 3 to 5 NTU) with low filterability (Table 1). Similar to the O₂ system, P16 + Ca1000 sample in the MnO₄ system had a higher initial turbidity (≈ 8 NTU) and improved particle settling (70% turbidity reduction) and filterability ($> 99\%$ Fe removed).

In the HOCl system (Fig. 2C), the initial turbidity of all suspensions (< 4 NTU) was systematically lower than the O₂ or MnO₄ systems. The Ref and Mn18 HOCl suspensions were light yellow with visible flocs that settled quickly and were effectively filtered ($\approx 90\%$), despite their low initial turbidity. The 150–750 μM Si samples were colloidally stable, similar to the O₂ and MnO₄ systems. When Ca was added to the Si solutions, turbidity removal improved (20%), but was lower than the Ref HOCl sample. The HOCl experiments in P solutions resembled the O₂ system more than the MnO₄ system, with 46% and 41% decreases in turbidity for P4 and P10 samples, but only 8% for the P16 sample. The impact of Ca in P solutions was similar in all HOCl, O₂ and MnO₄ systems, with the

P16 + Ca1000 sample displaying increased aggregation and sedimentation (40% turbidity decrease).

3.2. Mn/Fe solid ratios

In the O₂ system, the precipitate Mn/Fe ratio content was low (≤ 0.05) and varied with solution composition. The Mn/Fe ratio of the Ref experiment was 0.01 mol/mol, which doubled to 0.02 mol/mol in the Mn18 experiment, matching the doubled initial Mn concentration. The presence of Si and P increased the precipitate Mn content, with the Si150 and P16 samples having solids ratios of 0.03 mol/mol and 0.05 mol/mol, respectively. By contrast, Ca addition decreased the Mn/Fe ratio. The precipitate Mn content was only 0.02 mol/mol in the P16 + Ca1000 sample.

In MnO₄ system the Mn/Fe ratio ranged from 0.5 to 0.55, with no significant trends in the presence of Si, P and Ca. The higher Mn/Fe ratio relative to the O₂ and HOCl systems is attributed to the dosing of MnO₄, which increased the total Mn concentration.

In the HOCl system, the precipitate Mn/Fe ratio was higher than in the O₂ system, indicating more effective Mn uptake. The Mn/Fe ratio of the Ref and Mn18 experiments was 0.08 and 0.18 mol/mol, which was near the total Mn/Fe ratio dosed into solution. The presence of Si and P did not impact significantly the Mn/Fe ratio in the HOCl system (Table 1), with Mn/Fe ratios of ≈ 0.08 mol/mol for the Si350 and P16 samples. However, Ca addition decreased Mn uptake, leading to a Mn/Fe solids ratio of 0.05 mol/mol for the Si350 + Ca500 and P16 + Ca1000 samples.

3.3. Fe K-edge EXAFS spectroscopy

Principal component analysis (PCA) of the Fe K-edge EXAFS spectra of the entire data set (O₂, MnO₄, and HOCl systems) revealed a significant decrease in the indicator function (Fig. S2) with three independent components and a gradual plateau in the indicator function with increasing components. Based on the PCA results and the experimental conditions, we used three Fe(III) (oxyhydr)oxide standards in the linear combination fits (LCFs) of the experimental spectra: lepidocrocite (γ -FeOOH), 2-line ferrihydrite (2LFh), and an oxyanion-rich hydrous ferric oxide (oxy-HFO) that was produced by Fe(II) oxidation in the presence of P and that contains no Fe–Fe corner-sharing bonds (van Genuchten et al., 2014b). The LCF output is overlain to the data in Fig. 4 and results of the LCFs of the experimental spectra using lepidocrocite, 2LFh, and oxy-HFO are given Fig. 5.

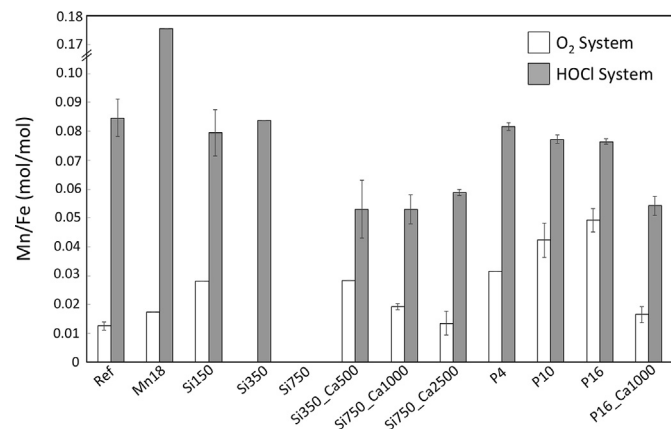


Fig. 3. Precipitate Mn/Fe ratio (mol/mol). Samples without data were colloiddally stable and could not to be separated with 0.45 μ m filters. The Mn/Fe ratio was between 0.5 and 0.55 for all the samples in MnO₄ system and is thus not given. Note the break in the y-axis from 0.10 to 0.17 mol/mol.

The Ref and Mn18 experiments in the O₂ system consisted of dominantly lepidocrocite ($>85\%$). The minor fraction ($<15\%$) of oxy-HFO determined in the LCFs of these samples likely arises from subtle differences in the structure of the lepidocrocite standard and the type of lepidocrocite formed in the experiments (van Genuchten et al., 2014b; Voegelin et al., 2010). Lepidocrocite formation was largely inhibited in the presence of Si, with the LCFs of all Si series samples returning fractions of 15–26% oxy-HFO and 72–82% 2LFh without clear trends in the fractions oxy-HFO and 2LFh with increasing Si or presence of Ca. In the P experiments, the LCFs indicated the formation of lepidocrocite, but its fraction depended on the P concentration (i.e. P/Fe ratio). Increasing P from 4 to 16 μ M decreased the lepidocrocite fraction from 64 to 27%, which was balanced by an increase in oxy-HFO from 16 to 37% (the 2LFh fraction was stable at $\approx 30\%$). The addition of Ca to the P16 solution increased the lepidocrocite fraction from 27 to 55% at the expense of oxy-HFO and 2LFh. This impact of Ca on the products of Fe(II) oxidation by O₂ in the P solutions is consistent with the sequential formation of Ca- and P-rich Fe(III) polymers (Voegelin et al., 2010) which remove P from solution with P/Fe ratios near 1, followed by lepidocrocite formation with excess Fe(II) after P is removed from solution.

In contrast to the O₂ experiments, no sample in the MnO₄ system consisted of lepidocrocite, regardless of solution composition. The LCFs indicated poorly-ordered Fe(III) precipitates formed in MnO₄ experiments, which had average structures consistent with mixtures of 2LFh and oxy-HFO (30–73% oxy-HFO, 25–69% 2LFh). Increasing the Si concentration from 150 to 750 μ M increased the fraction of oxy-HFO from 32 to 60%, with 2LFh making up the remainder. The Fe(III) precipitates formed from Fe(II) oxidation by MnO₄ in P solutions were similar to those in Si solutions, with the LCFs yielding mixtures of 2LFh and oxy-HFO without clear trends in the presence of Ca.

In the HOCl system, lepidocrocite was not detected in any sample. The LCFs of the Ref sample yielded 53% oxy-HFO and 40% 2LFh, whereas the Mn18 sample consisted of 40% oxy-HFO and 54% 2LFh (Fig. 5). Although P and Si increased the fraction of poorly-ordered Fe(III) precipitates in the O₂ system, the analogous trend was not observed in the HOCl system. No trends in the fractions of 2LFh and oxy-rich HFO with increasing Si or P were observed in the HOCl samples. Comparing the LCFs across all oxidants (i.e. O₂, MnO₄, and HOCl) reveals that Si and P impacted Fe(III) speciation in the O₂ experiments more than in MnO₄ and HOCl experiments.

3.4. Mn K-edge XANES spectroscopy

The Mn K-edge XANES LCFs of the Ref O₂ sample (Fig. 6, Table 2) indicated that Mn(III) was the dominant species ($96 \pm 3\%$) in the solids, consistent with the absorption maximum near 6556 eV. However, the Si150 sample displayed an absorption maximum at lower X-ray energy (6552 eV) and the LCFs indicated Mn(II) was the dominant species (Mn(II) = $75 \pm 2\%$, Mn(III) = $26 \pm 4\%$). The trend in increased Mn(II) in the presence of oxyanions was also observed in the P16 experiment, which consisted of $85 \pm 3\%$ Mn(II), with Mn(III) making up the remainder. When Ca was added to the P16 electrolyte, the LCFs indicated a significant decrease in solid-associated Mn(II) ($52 \pm 3\%$) and an increase in Mn(III) ($45 \pm 5\%$). The presence of Mn(IV) was not supported by the LCFs of any O₂ samples.

The XANES spectra of the MnO₄ samples were largely independent of solution chemistry, with $>98\%$ Mn(IV) detected by the LCFs in all samples (absorption maximum near 6558 eV). While the LCFs returned a small fraction of Mn(III) in some samples ($<20\%$), the standard deviation was nearly as high as the fit-derived value (Table 2). No clear trends in the Mn oxidation state with Si, P, or Ca

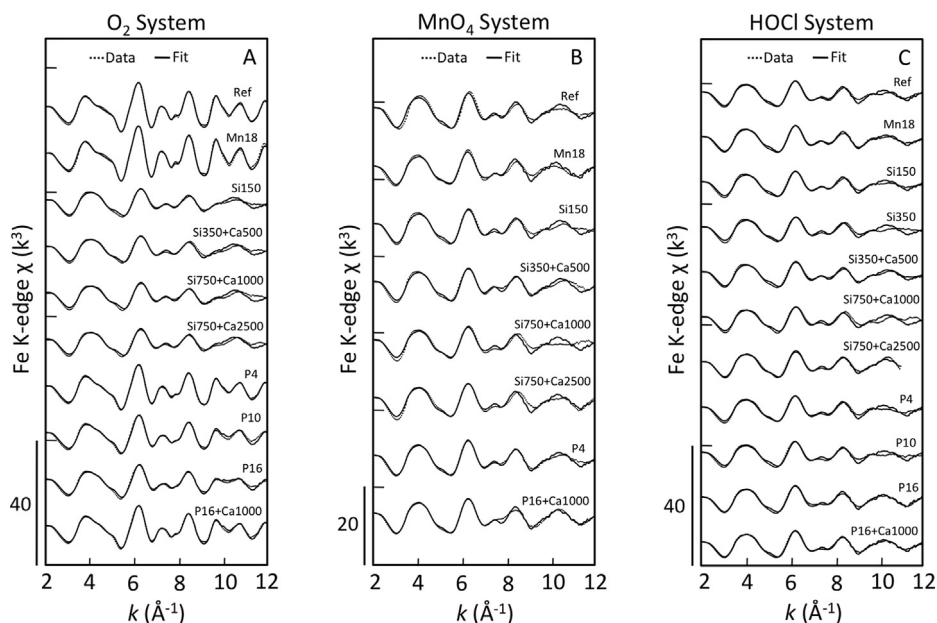


Fig. 4. Fe K-edge EXAFS spectra of precipitate samples (dotted lines) and output of linear combination fits (solid lines) using lepidocrocite, 2-line ferrihydrite, and oxyanion-rich hydrous ferric oxide.

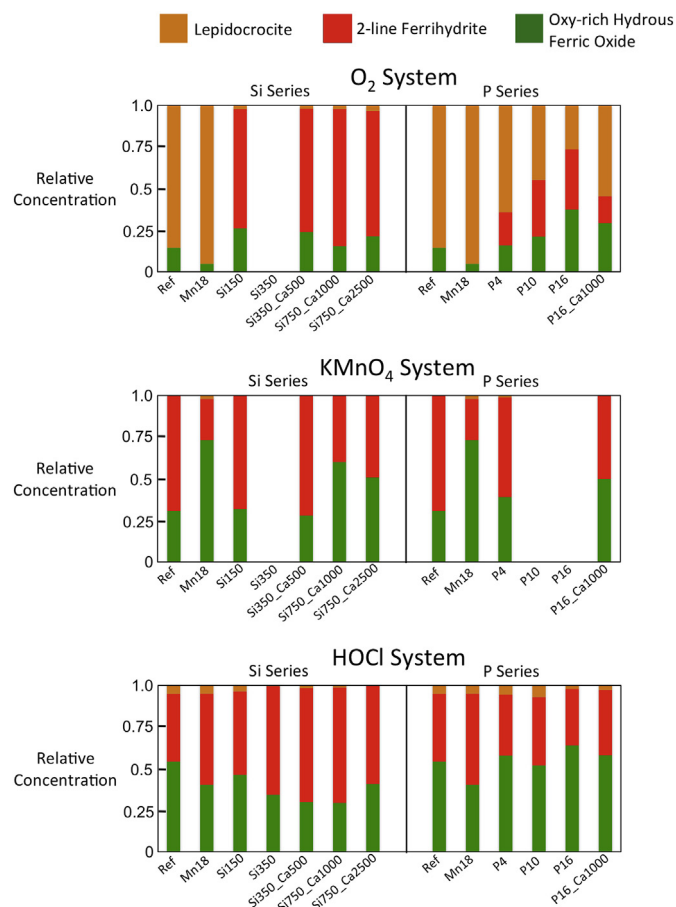


Fig. 5. Relative concentrations of lepidocrocite (brown bars), 2-line ferrihydrite (red bars), and oxyanion-rich hydrous ferric oxide (green bars) derived by linear combination fits for each precipitate sample. Samples without data were colloidally stable and could not to be separated with $0.45 \mu\text{m}$ filters. (For interpretation of the references to color in this figure legend, the reader is referred to the Web version of this article.)

were detected in the LCFs of the MnO_4 samples. The presence of residual, unreacted Mn(VII), which has a prominent pre-edge peak near 6541 eV , was not supported by the XANES spectra.

Co-oxidation of Fe(II) and Mn(II) by HOCl produced primarily Mn(III) in the Ref and Mn18 samples, with a slight increase in the Mn(IV) fraction from $15 \pm 10\%$ in the Ref sample to $23 \pm 11\%$ in the Mn18 sample. The LCFs of the Si150 sample indicated that Mn(III) remained the dominant solid-phase Mn species ($>85\%$). At P concentrations of 4 and $16 \mu\text{M}$, the solid-phase Mn(II) fraction increased from 9 ± 5 to $41 \pm 4\%$. When Ca was added to the P16 solution, the solid-phase Mn(II) fraction decreased from 41 ± 4 to $14 \pm 5\%$. A similar decrease in Mn(II) fraction in favor of Mn(III) was observed in the O_2 experiments when Ca was added to the P16 solution.

3.5. Mn K-edge EXAFS spectroscopy

3.5.1. O_2 experiments

In Fig. 7, the Mn K-edge EXAFS spectra of samples produced in the O_2 , MnO_4 , and HOCl experiments are shown alongside the spectra of Mn standards. The Ref O_2 sample, which was found by the LCFs to be dominantly Mn(III), differed relative to the other spectra in Fig. 7, including the aqueous Mn(II), bixbyite ($\alpha\text{-Mn}_2\text{O}_3$) and $\delta\text{-MnO}_2$ standards. In particular, the first oscillation from 3 to 5.5 \AA^{-1} became a doublet, which is not present in other Mn(III)-bearing material (e.g. groutite, manganite, feitnchtite) (Manceau et al., 2012). Furthermore, the next major peaks at 6.2 and 7.5 \AA^{-1} in the Ref O_2 sample are out of phase with the standards, which suggests a unique Mn coordination environment. In the presence of P and Si, the EXAFS oscillations for the O_2 samples match more closely those of aqueous Mn(II), which is consistent with the XANES-derived predominance of Mn(II) in these samples.

Shell-by-shell fits of the Fourier-transformed Mn K-edge EXAFS spectrum of the Ref O_2 sample (Fig. 8, Table 3) returned an Mn–O interatomic distance ($R_{\text{Mn-O}}$) of $1.93 \pm 0.02 \text{ \AA}$ and an Mn–O coordination number ($\text{CN}_{\text{Mn-O}}$) of 1.9 ± 0.5 , which is lower than the theoretical CN of 6 for octahedrally coordinated Mn(III). These fit-derived $R_{\text{Mn-O}}$ and $\text{CN}_{\text{Mn-O}}$ values matched the first shell fits of

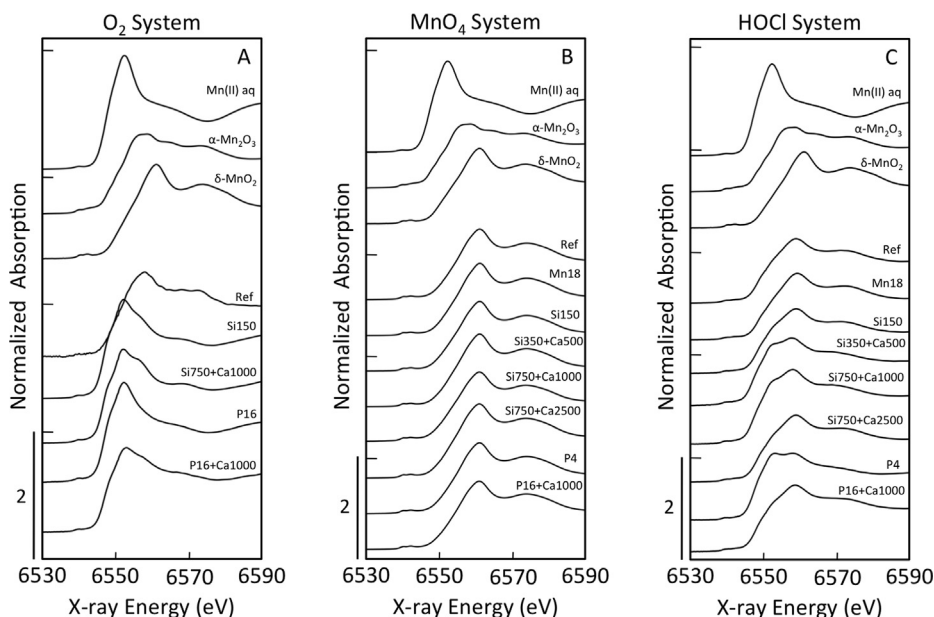


Fig. 6. Mn K-edge XANES spectra for precipitate samples formed in the O₂ (left panel), MnO₄ (middle panel) and HOCl (right panel) experiments. The experimental data is plotted below Mn(II), Mn(III), and Mn(IV) standards.

Table 2
Summary of XANES LCF results.

Oxidant	Experiment Code	% Mn ²⁺	% Mn ³⁺	% Mn ⁴⁺
O ₂ System	Ref	<1	96 ± 3	<1
	Si150	75 ± 2	26 ± 4	<1
	Si750 + Ca1000	65 ± 3	35 ± 5	<1
	P16	85 ± 3	20 ± 4	<1
	P16 + Ca1000	52 ± 3	45 ± 5	<1
MnO ₄ System	Ref	<1	8 ± 8	106 ± 15
	Mn18	<1	6 ± 7	109 ± 15
	Si150	<1	7 ± 8	105 ± 14
	Si350 + Ca500	<1	8 ± 9	108 ± 14
	Si750 + Ca1000	<1	16 ± 6	99 ± 16
	Si750 + Ca2500	<1	17 ± 8	102 ± 14
	P4	<1	10 ± 7	104 ± 15
	P16 + Ca1000	<1	13 ± 6	98 ± 15
HOCl System	Ref	5 ± 4	84 ± 16	15 ± 10
	Mn18	<1	79 ± 15	23 ± 11
	Si150	11 ± 5	85 ± 18	10 ± 11
	Si750 + Ca1000	33 ± 8	85 ± 12	<1
	Si750 + Ca2500	27 ± 6	95 ± 11	<1
	P4	9 ± 5	87 ± 18	11 ± 12
	P16	41 ± 4	63 ± 11	3 ± 4
	P16 + Ca1000	14 ± 5	88 ± 18	10 ± 11

bixbyite ($R_{\text{Mn-O}} = 1.92 \pm 0.02 \text{ \AA}$, $\text{CN}_{\text{Mn-O}} = 2.4 \pm 0.5$) and are consistent Jahn-Teller distorted Mn(III) octahedra. Fits of the second shell of the Ref O₂ sample resulted in a $\text{CN}_{\text{Mn-Mn/Fe}} = 2.8 \pm 1.1$ and $R_{\text{Mn-Mn/Fe}} = 3.04 \pm 0.02 \text{ \AA}$. This $R_{\text{Mn-Mn/Fe}}$ is significantly shorter than the edge-sharing Mn–Mn bond in bixbyite (Table 3) and longer than the edge-sharing Mn–Mn bond in groutite (Wyckoff, 1963). However, the fit-derived $R_{\text{Mn-Mn/Fe}}$ value for this sample is in good agreement with the edge-sharing Fe–Fe bond length in the Fe(III) precipitates that formed in this sample (i.e. lepidocrocite, $R_{\text{Fe-Fe}} = 3.07 \pm 0.01 \text{ \AA}$, Table S1).

3.5.2. MnO₄ experiments

The Mn K-edge EXAFS spectra of MnO₄ samples were similar regardless solution composition, with all samples resembling the

EXAFS spectrum of the δ -MnO₂ standard. All experimental EXAFS spectra contained the characteristic staircase feature from 4 to 6 \AA^{-1} indicative of MnO₂ minerals (Manceau et al., 2012), which implies that Mn(II) and Fe(II) co-oxidation by MnO₄ in a variety of solutions leads to solid-phase Mn in a MnO₂-like bonding environment.

Shell-by-shell fits of the Ref MnO₄ sample, which contained <10% Mn(III) (Table 2), indicated a Mn–O coordination shell of $\text{CN}_{\text{Mn-O}} = 5.2 \pm 0.9$ and $R_{\text{Mn-O}} = 1.91 \pm 0.01 \text{ \AA}$. These fit-derived values are in excellent agreement with the first shell fits of the δ -MnO₂ standard (Table 3) and are representative of Mn(IV) in octahedral coordination. The second shell fit of the Ref MnO₄ sample returned values of $\text{CN}_{\text{Mn-Mn/Fe}} = 3.2 \pm 0.4$ and $R_{\text{Mn-Mn/Fe}} = 2.89 \pm 0.01 \text{ \AA}$, which also matches the fits δ -MnO₂ standard (Table 3) and is consistent with edge-sharing MnO₆ octahedra. Furthermore, this fit-derived $R_{\text{Mn-Mn/Fe}}$ value is considerably shorter than the fit-derived $R_{\text{Mn-Mn/Fe}}$ of the Ref O₂ sample and is also shorter than the edge-sharing Fe–Fe bond in Fe(III) (oxyhydr) oxide minerals (Manceau and Combes, 1988). Interestingly, the shell-by-shell fits of the Ref MnO₄ sample and the MnO₄ sample generated in the highest oxyanion solution (i.e. Si750 + Ca2500) were identical within fit-derived standard errors (Table 3). This result suggests that co-occurring oxyanions do not modify the structure of co-precipitated MnO₂ solids as much as Fe(III) precipitates, which is attributed to the lower affinity of oxyanions for MnO₂ surfaces than Fe(III) (oxyhydr)oxides (van Genuchten and Peña, 2016a).

3.5.3. HOCl experiments

The EXAFS spectra of the Ref and Mn18 samples in the HOCl system, which consisted of primarily Mn(III) (Table 3), were nearly identical. Both Ref and Mn18 spectra displayed a split oscillation from 3 to 5 \AA^{-1} , which is similar to that of the Ref O₂ sample, but the split in this oscillation was less prominent in the HOCl samples. The Ref and Mn18 HOCl samples also exhibited an asymmetric oscillation near 6.5 \AA^{-1} that was less pronounced or absent from the EXAFS spectra of other samples and standards (Fig. 7). In the presence of P and Si, some features in the EXAFS spectra changed,

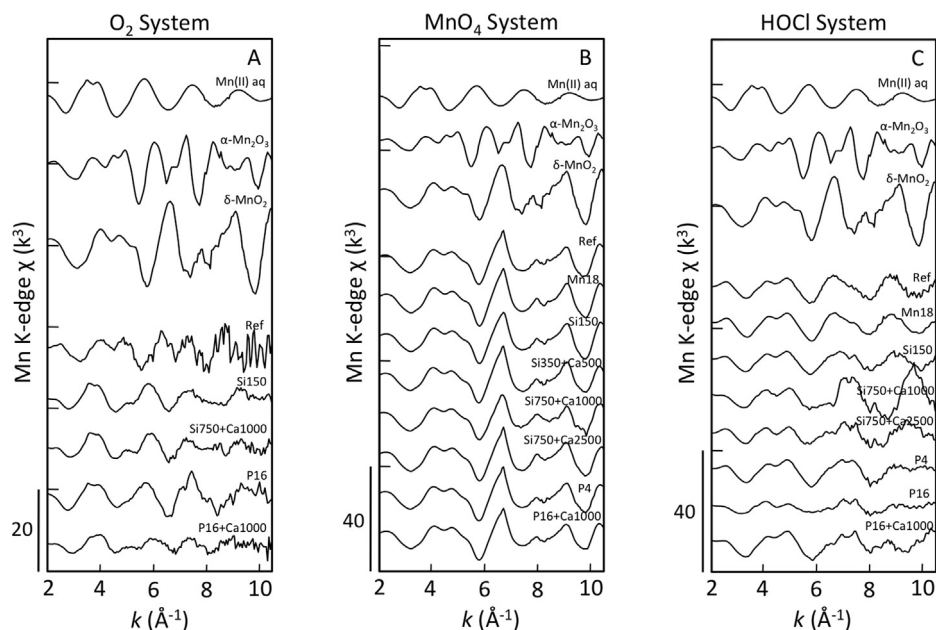


Fig. 7. Mn K-edge EXAFS spectra for precipitate samples formed in the O₂ (left panel), MnO₄ (middle panel) and HOCl (right panel) experiments. The experimental data is plotted below Mn(II), Mn(III), and Mn(IV) standards.

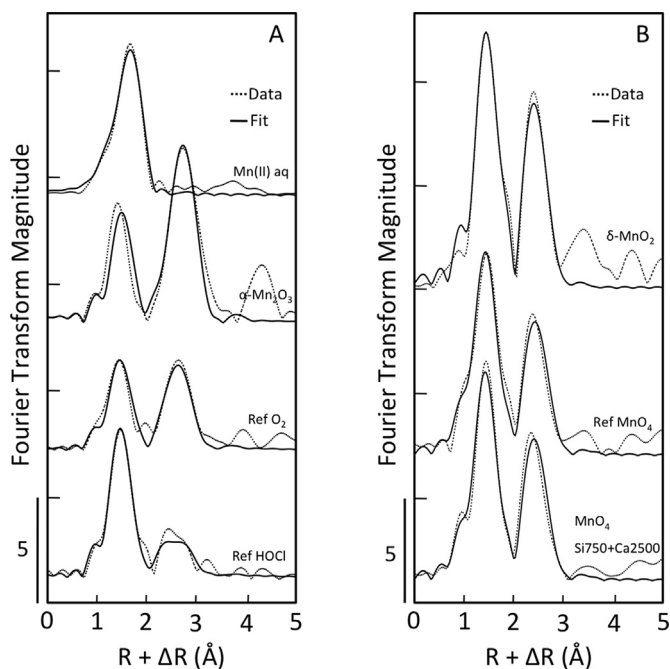


Fig. 8. Fourier-transformed Mn K-edge EXAFS spectra of precipitate samples (dotted lines) overlain to the output of shell-by-shell fits.

including the disappearance of the asymmetric oscillation near 6.5 Å, but the first oscillation from 3 to 5 Å⁻¹ was still split. The similarity of key EXAFS features across all HOCl samples regardless of the presence (e.g. Si150, P4) or absence (Ref, Mn18) of oxyanions is consistent with the XANES LCFs, which identified Mn(III) as the predominant Mn oxidation state in all HOCl samples (Table 2).

Shell-by-shell fits of the Fourier-transformed EXAFS spectrum of the Ref HOCl sample (Table 3) revealed a first shell Mn–O coordination environment similar to the Ref O₂ sample, with CN_{Mn–O} = 2.4 ± 0.4 and R_{Mn–O} = 1.91 ± 0.01 Å, which is consistent

with Jahn-Teller distorted Mn(III) octahedra. Fits of the second shell of the Ref HOCl sample returned values of 1.7 ± 0.4 for CN_{Mn–Mn/Fe} and 3.01 ± 0.02 Å for R_{Mn–Mn/Fe}. Similar to the O₂ system, the second shell fits of the Ref HOCl sample produced a R_{Mn–Mn/Fe} value that is shorter than the edge-sharing Mn–Mn bond in Mn(III)-bearing minerals. However, the R_{Mn–Mn/Fe} for the HOCl sample is in good agreement with the Fe–Fe bond length for edge-sharing FeO₆ octahedra in Fe(III) precipitates that formed in this sample (i.e. hydrous ferric oxide, R_{Fe–Fe} = 3.05 ± 0.01 Å, Table S1).

4. Discussion

4.1. Effect of oxidant and solution chemistry on Fe(III) speciation and particle aggregation

4.1.1. Fe(II) oxidation in O₂, MnO₄, and HOCl ref experiments

Comparison of the Ref experiments across all oxidants shows that Fe(II) and Mn(II) co-oxidation by O₂ and HOCl produced suspensions that aggregated rapidly and that were separated by gravitational settling or filtering easily, whereas the MnO₄ Ref experiment generated a colloiddally stable suspension. However, Fe(III) speciation differed between Ref O₂ and Ref HOCl experiments, with O₂ producing lepidocrocite and both HOCl and MnO₄ producing poorly-crystalline Fe(III) precipitates. These differences in aggregation and Fe(III) speciation with oxidant can be explained by the different Fe(II) reaction rates with O₂, HOCl, and MnO₄ and the different end-products of each reaction. The Fe(II) oxidation rate by O₂ depends strongly on pH (van Beek et al., 2016; van Beek et al., 2012; Vries et al., 2017), but at circumneutral pH is orders of magnitude lower than HOCl and MnO₄ (Ghurye and Clifford, 2001; Knocke et al., 1991; Stumm and Morgan, 1996). Although our experiments were designed to allow for complete Fe(II) oxidation in the O₂ experiments, Fe(II) reactions with O₂ are not instantaneous, which ensures that freshly-oxidized Fe(III) precursors form in the presence of Fe(II). Aqueous Fe(II) catalyzes the rapid transformation of poorly-ordered Fe(III) precipitates into lepidocrocite, which was the dominant Fe(III) phase of the Ref O₂ experiment (Pedersen et al., 2005). By contrast, the reaction rate of HOCl and MnO₄

Table 3
Summary of shell fits of Mn-bearing standards and precipitate samples.

Experiment Code	Atomic Pairs	CN	R (Å)	σ^2 (Å ²)	ΔE_0 (eV)	R-Factor
Aqueous Mn(II)	Mn–O	7.0 (0.6)	2.18 (0.01)	0.010 (0.001)	–11.0 (1.0)	0.015
α -Mn ₂ O ₃	Mn–O	2.4 (0.7)	1.92 (0.02)	0.004 (0.002)	–16.7 (1.8)	0.041
	Mn–Mn1	4.8 (2.3)	3.10 (0.03)	0.009 (0.004)		
	Mn–Mn2	3.4 (1.7)	3.53 (0.04)	σ^2 (Mn–Mn1)		
δ -MnO ₂	Mn–O	4.4 (1.0)	1.90 (0.01)	0.001 (0.001)	–17.6 (2.7)	0.047
	Mn–Mn	4.3 (0.6)	2.88 (0.02)	0.007		
Ref O ₂	Mn–O	1.9 (0.5)	1.93 (0.02)	0.004 (0.003)	–11.4 (3.0)	0.067
	Mn–Mn/Fe	2.8 (1.1)	3.04 (0.02)	0.009 (0.003)		
Ref HOCl	Mn–O	2.4 (0.4)	1.91 (0.01)	0.002 (0.001)	–10.0 (2.1)	0.032
	Mn–Mn/Fe	1.7 (0.4)	3.01 (0.02)	0.01		
Ref MnO ₄	Mn–O	5.2 (0.9)	1.91 (0.01)	0.005 (0.002)	–16.7 (2.1)	0.031
	Mn–Mn/Fe	3.2 (0.4)	2.89 (0.01)	0.007		
MnO ₄	Mn–O	4.9 (0.7)	1.90 (0.01)	0.004 (0.001)	–17.3 (1.7)	0.020
Si750 + Ca1000	Mn–Mn/Fe	3.3 (0.3)	2.87 (0.01)	0.007		

CN represents the coordination number, R the interatomic distance, σ^2 the mean squared atomic displacement and ΔE_0 represents the change in threshold energy. The passive electron reduction factor, S_0^2 , was fixed at 0.7. Fitting parameters allowed to float are accompanied by fit-determined standard errors in parenthesis, while constrained parameters appear without a parenthesis. All fits were carried out from 1 to 3.5 Å in R+ ΔR -space. The number of independent point (N_{IDP}) in the fits was 13.4 and the number of variables (N_{var}) was 4–9.

with Fe(II) is high enough that aqueous Fe(II) is too unstable to catalyze the transformation of freshly-formed Fe(III) to lepidocrocite, leading to the persistence of poorly-ordered Fe(III) precipitates. Although Fe(III) speciation was similar in the Ref HOCl and MnO₄ experiments, the Ref MnO₄ solids contained a major fraction of MnO₂ that did not form in the O₂ and HOCl experiments. The presence of MnO₂ likely enhances the colloidal stability of the MnO₄ samples because of the much lower point of zero charge of MnO₂ (≈ 2 –3) compared to lepidocrocite and poorly-ordered Fe(III) precipitates (≈ 7 –8) (Sposito, 2008). At circumneutral pH, suspensions containing MnO₂ will have a strong negative charge, preventing aggregation, whereas suspensions of Fe(III) precipitates will be near the optimum pH to induce aggregation (Sposito, 2008).

4.1.2. Impact of ionic composition

Solution chemistry was found to alter both the suspension stability and Fe(III) speciation, with different impacts depending on the Fe(II) oxidant and ionic composition. The Fe(III) speciation in the O₂ samples was impacted the most by solution composition, but similar trends were observed in the MnO₄ and HOCl experiments. The presence of oxyanions in the O₂ samples decreased particle aggregation and resulted in a transition from lepidocrocite to poorly-ordered Fe(III) precipitates. Oxyanions, such as Si and P, bind strongly to Fe(III) precipitate surfaces during Fe(III) polymerization, which modifies two key properties of the suspension. First, by binding strongly to crystal growth sites on the Fe(III) precipitate surface, oxyanions inhibit the formation of crystalline Fe(III) minerals (i.e. lepidocrocite), leading to the persistence of poorly-ordered Fe(III) precipitates with a large specific surface area (van Genuchten et al., 2014b; Voegelin et al., 2010). Second, sorption of oxyanions leads to negatively charged Fe(III) precipitate surfaces, even in the case of Si, which is uncharged in solution circumneutral pH (Delaire et al., 2016; Kanematsu et al., 2013). Therefore, oxyanion sorption generates particles with highly negative surface charge that are less likely to aggregate. Both consequences of co-occurring oxyanions during Fe(III) precipitation (i.e. changes in suspension aggregation and Fe(III) speciation) were observed in the O₂ experiments. These effects were less pronounced in the MnO₄ experiments since the Ref MnO₄ suspension was already colloidal stable and consisted of poorly-ordered Fe(III) precipitates even in the absence of Si and P.

The presence of Ca can counteract some of the oxyanion effects, particularly with respect to particle surface charge. Ca addition enhanced aggregation (i.e. settling and filterability) in nearly every O₂, HOCl and MnO₄ experiment, with stronger impact in P solutions than Si. The pronounced impact of Ca in P solutions is attributed to the formation of Ca–O–P linkages during Fe(III) polymerization that enhance particle aggregation by neutralizing more effectively the negative surface charge of P-rich Fe(III) precipitates (Senn et al., 2015; van Genuchten et al., 2014a; Voegelin et al., 2010). The presence of Ca was also important to enhancing the aggregation of MnO₄ suspensions, which is explained by positively charged Ca neutralizing the negatively charged MnO₂ produced in the MnO₄ experiments.

4.2. Behavior of Mn(II) during co-oxidation with Fe(II)

4.2.1. Mn(II) removal in O₂, MnO₄, and HOCl ref experiments

A visual representation of the structure and composition of the solids formed in the Ref experiments is given in Fig. 9. The Ref O₂, MnO₄ and HOCl experiments were performed in solutions with the least ionic complexity and form the baseline for comparing Mn(II) removal in the simulated groundwater solutions. In the Ref O₂ experiment, the Mn/Fe solids ratio was ≈ 0.01 mol/mol (i.e. $\approx 10\%$ Mn(II) removal) and the XANES LCFs indicated solid-phase Mn was dominantly Mn(III). Shell-by-shell fits of the Ref O₂ sample were consistent with a first shell Mn(III)–O coordination environment and a second shell that consisted of Mn–Mn/Fe atomic pairs at $R = 3.04 \pm 0.02$ Å. This R-value matches that of edge-sharing FeO₆ octahedra in the Fe(III) precipitates formed in this sample (Table S1). Therefore, Mn(II) removal in the Ref O₂ experiment likely occurs via Mn(II) oxidation to Mn(III) by the reactive Fenton-type oxidants produced during Fe(II) oxidation by O₂ (*O_2 , Fe(IV)) and subsequent (partial) incorporation into the resulting Fe(III) precipitate. This Mn(II) removal mechanism has been observed in experiments that dosed Fe(II) slowly by Fe(0) electrolysis into air-saturated solutions of Mn(II), allowing Fe(II) and Mn(II) co-oxidize by O₂ (van Genuchten and Pena, 2017).

The Ref MnO₄ experiment had a high Mn/Fe solids ratio of >0.5 mol/mol, which matches the total Mn/Fe ratio dosed into the initial solution. The XANES LCFs of the Ref MnO₄ sample indicated

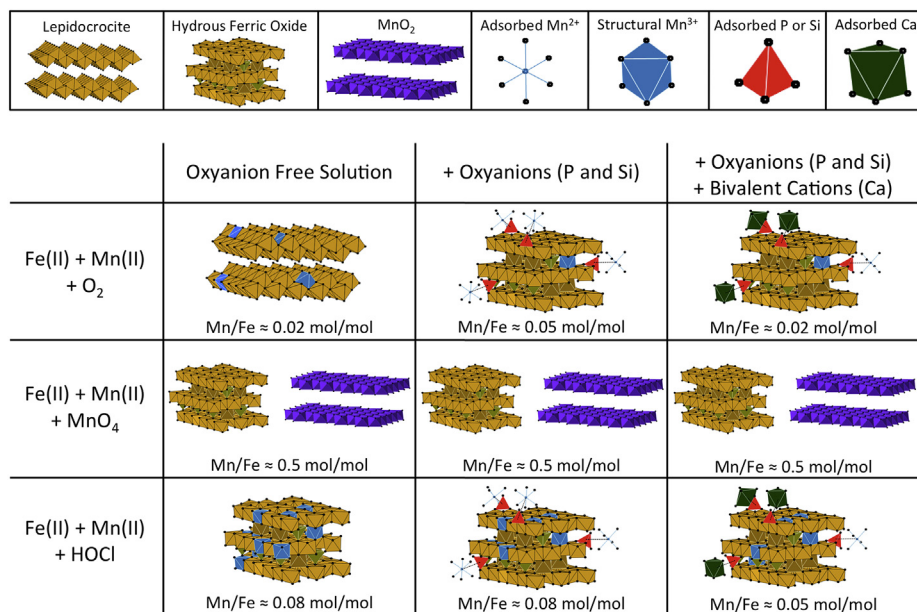


Fig. 9. Visual representations and Mn/Fe ratios of the experimental solids derived from the wet chemical measurements and XAS analyses. We expect that sorbed Mn(II) increased in the oxyanion experiments due to Mn(II) interactions with P and Si bound to the Fe(III) precipitate. We did not include P or Si oxyanions bound to the Fe(III) precipitates in the MnO₄ panels since Mn(II) was not detected in these samples.

Mn was present as Mn(IV). The line shape and position of the Mn K-edge EXAFS spectrum and the shell-by-shell fitting output of the Ref MnO₄ sample indicated an Mn coordination environment similar to the δ-MnO₂ standard. The formation of nanoscale MnO₂ by reaction of Mn(II) and MnO₄ has been well documented in many studies (Knocke et al., 1991; Lee et al., 2011) and our results suggest that the presence of Fe(II) and other background ions in the Ref MnO₄ experiment did not alter this reaction pathway.

Effective removal of approximately 80% of the initial Mn(II) was observed in the Ref HOCl experiment, leading to a Mn/Fe solids ratio of ≈0.08 mol/mol, which was significantly higher than the Ref O₂ sample. The XANES LCFs of the Ref HOCl sample indicated that solid-phase Mn was dominantly Mn(III). Similar to the O₂ system, the shell-by-shell fits of the Ref HOCl sample were consistent with a first shell Mn(III)–O coordination environment and second shell that consisted of Mn–Mn/Fe atomic pairs at an R-value (3.01 ± 0.02 Å) that is not found in Mn(III) (oxyhydr)oxide minerals. However, this R-value is similar to that of the edge-sharing Fe octahedra in the Fe(III) precipitates that formed in this sample (3.05 ± 0.01 Å, Table S1). Therefore, we propose that Mn(II) removal in the Ref HOCl experiment proceeds by a single electron transfer from Mn(II) to Mn(III), with Mn(III) stabilized by (partial) incorporation into co-precipitating Fe(III) (oxyhydr)oxides. While a similar Mn(II) removal pathway has been documented for Mn(II) and Fe(II) co-oxidation by H₂O₂, this pathway is inconsistent with previous research investigating Mn(II) removal by chlorination, which report the formation of Mn(IV) species (Allard et al., 2013; Hao et al., 1991). In our experiments, the precipitation of Fe(III) during Mn(II) oxidation likely stabilizes the initial Mn(III) product by incorporation into the solid phase, which prevents subsequent Mn(III) oxidation to Mn(IV).

4.2.2. Impact of ionic composition

A visual representation of the impact of oxyanions and bivalent cations on the structure and composition of the precipitates formed by Fe(II) and Mn(II) co-oxidation is given in Fig. 9. Solution

composition modified the uptake and removal mechanism of Mn(II) in many experiments, with the most pronounced impacts in the O₂ and HOCl systems. Based on the XANES LCFs and Mn K-edge EXAFS spectra, Mn(II) was removed by reaction with MnO₄ to form nanoscale MnO₂ in every experiment in the MnO₄ system, regardless of solution composition. However, in the O₂ and HOCl experiments, Si and P increased the fraction of solid-phase Mn(II). For example, whereas <5% Mn(II) was present in the Ref O₂ and HOCl samples, the P16 samples in the O₂ and HOCl systems consisted of 85 ± 3 and 41 ± 4% Mn(II), respectively. The impact of Si was weaker than P, but still increased the Mn(II) fraction in the Si150 sample in the O₂ system to 75 ± 2%. Furthermore, the increased fraction of sorbed Mn(II) in the O₂ experiments coincided with an increase in Mn/Fe solids ratio, particularly in the P experiment (Mn/Fe_{Ref} = 0.01 mol/mol, Mn/Fe_{P16} = 0.05 mol/mol). These results indicate that P, and Si to a lesser extent, can enhance Mn(II) sorption when Mn(II) oxidation is incomplete. The enhanced Mn(II) removal in the presence of oxyanions can be explained by the interaction between positively charged Mn(II) and negatively charged surfaces of oxyanion-rich Fe(III) precipitates. The more pronounced impact of P relative to Si could arise from direct Mn(II)–O–P bonding on the Fe(III) precipitate surface (i.e. ternary complexes), analogous to Ca–O–P linkages.

In contrast to the effect of oxyanions, the presence of Ca in Si and P solutions systematically decreased the fraction of solid-phase Mn(II) in both O₂ and HOCl experiments. The impact of Ca was most pronounced in the P16 solutions, with decreases in the Mn(II) fraction from 85 ± 3 to 20 ± 4% in the O₂ system and from 41 ± 4 and 14 ± 5% in the HOCl system. The Ca-induced decrease in sorbed Mn(II) was coupled to a decrease in the Mn/Fe solids ratio (Fig. 3), which suggests that Ca can compete effectively with Mn(II) for sorption sites, especially in the case of P-rich Fe(III) precipitates. This conclusion is consistent with the similar ionic potential (charge/ionic radius) of Mn(II) (IP_{Mn(II)} ≈ 24) and Ca (IP_{Ca} ≈ 20) ions, which suggests similar sorption reactivity between Mn(II) and Ca.

4.3. Conclusions and implications for water treatment

We found that the composition of water and the identity of the oxidant strongly determines the macroscopic and molecular-scale characteristics of Fe and Mn bearing precipitates generated by Fe(II) and Mn(II) co-oxidation. The higher Mn/Fe ratio of the precipitates produced with MnO_4 or HOCl indicates that the Mn removal mechanism will differ between the typical aeration—rapid sand filtration type groundwater treatment systems that rely on bacteria and surface catalysts for Mn(II) removal (Bruins et al., 2015) and the ones that use strong oxidants such as KMnO_4 and NaOCl. In the prior case, Mn removal will take place deeper in the filter bed, whereas Mn is expected to precipitate in the supernatant storage with KMnO_4 and NaOCl, resulting in accumulation of Mn bearing solids in the top sand filter layer.

Our study shows that the addition of Ca counteracts the negative effect of oxyanions and enhances the settling and filterability of Fe and Mn bearing precipitates. Thus, water treatment utilities that plan to implement softening at Fe/Mn removal plants should consider placing softening reactors after Fe/Mn removal to avoid colloidal stable suspensions arising from solutions low in bivalent cations. If colloidal stable suspensions are unavoidable, low pressure membrane systems (microfiltration/ultrafiltration) may replace rapid sand filters for effective removal of colloidal precipitates, but the fouling of membranes will be a critical issue. Precipitates can foul the membranes in different ways, depending on particle size. Particle sizes larger than the membrane pores will deposit on membrane surfaces, resulting in cake layer formation, which is often easily reversible (Floris et al., 2016). However, smaller particles can deposit in the membrane internal structure, resulting in undesirable pore entrapment and pore narrowing, which severely decreases the flux over time (irreversible fouling).

With respect to contaminant removal during treatment, the formation of MnO_2 by MnO_4 addition should not be overlooked. The characterization data in the MnO_4 experiments indicated that the Mn solids were structurally similar to $\delta\text{-MnO}_2$, a nanoscale MnO_2 mineral. These types of Mn(IV) oxides have remarkable reactivity with respect to sorption of a wide variety of toxic heavy metals (e.g. Cd(II), Pb(II), Cu(II), Ni(II)) (Peña et al., 2015; Pena et al., 2010; Villalobos, 2015). For example, the Pb/Mn solids ratio for $\delta\text{-MnO}_2$ can reach 0.4 mol/mol (Villalobos et al., 2005), which is partly due to highly reactive Mn(IV) vacancies in MnO_2 sheets (Lanson et al., 2002). In our study, MnO_4 was investigated primarily because it improves the kinetics of Fe(II), Mn(II) and As(III) oxidation. However, our results suggest that Fe(II) oxidation by MnO_4 and the production of mixtures of Fe(III) precipitates and MnO_2 would be ideal for concurrent treatment of As(III) and heavy metals. This result is particularly important for the co-removal of As(III) and Cd(II), which can often occur simultaneously in polluted environments (Perera et al., 2016), since Cd(II) removal by Fe(III) precipitates is much less effective than MnO_2 (van Genuchten and Peña, 2016b).

Acknowledgement

This research is co-financed with PPS-funding from the Top-consortia for Knowledge & Innovation (TKI's) of the Ministry of Economic Affairs and Climate. AA acknowledges support from Evides Waterbedrijf. CMvG acknowledges funding from a NWO Veni grant. The authors want to thank Luuk de Waal of KWR, Simon Mueller of Evides and Martijn Eikelboom of Wageningen University for their support during the experiments. We thank Ryan Davis at SSRL and Dipanjan Banerjee at ESRF for assistance during XAS data collection. Use of SSRL, SLAC National Accelerator Laboratory, was

supported by the U.S. Department of Energy, Office of Science, Basic Energy Sciences, under Contract No. DE-AC02-76SF00515.

Appendix A. Supplementary data

Supplementary data to this article can be found online at <https://doi.org/10.1016/j.watres.2019.06.036>.

References

- Ahmad, A., Kools, S., Schriks, M., Stuyfzand, P., Hofs, B., 2015. Arsenic and Chromium Concentrations and Their Speciation in Groundwater Resources and Drinking Water Supply in the Netherlands. KWR Water Cycle Research Institute, Nieuwegein, The Netherlands, p. 78.
- Ahmad, A., Cornelissen, E., van de Wetering, S., van Dijk, T., van Genuchten, C., Bundschuh, J., van der Wal, A., Bhattacharya, P., 2018. Arsenite removal in groundwater treatment plants by sequential Permanganate—Ferric treatment. *J. Water Process Eng.* 26, 221–229.
- Allard, S., Fouché, L., Dick, J., Heitz, A., von Gunten, U., 2013. Oxidation of Manganese(II) during Chlorination: Role of Bromide.
- Borsboom, M., Bras, W., Cerjak, I., Detollenaere, D., van Loon, D., Goedtkindt, P., Konijnenburg, M., Lassing, P., Levine, Y., Munneke, B., Oversluizen, M., van Tol, R., Vlieg, E., 1998. The Dutch-Belgian beamline at the ESRF. *J. Synchrotron Radiat.* 5, 518–520.
- Bruins, J.H., Petrussevski, B., Slokar, Y.M., Kruijthof, J.C., Kennedy, M.D., 2015. Manganese removal from groundwater: characterization of filter media coating. *Desalination Water Treat.* 55 (7), 1851–1863.
- de Moel, P.J., Verberk, J.Q.J.C., van Dijk, J.C., 2006. Drinking Water: Principles and Practices, Delft, The Netherlands.
- Delaire, C., van Genuchten, C., Amrose, S., Gadgil, A., 2016. Bacteria attenuation by iron electrocoagulation governed by interactions between bacterial phosphate groups and Fe(III) precipitates. *Water Res.* 103, 74–82.
- Diem, D., Stumm, W., 1984. Is dissolved Mn^{+2} being oxidized by O_2 in absence of Mn-bacteria and surface catalysts? *Geochem. Cosmochim. Acta* 48, 1571–1573.
- Floris, R., Nijmeijer, K., Cornelissen, E.R., 2016. Removal of aqueous nC_{60} fullerene from water by low pressure membrane filtration. *Water Res.* 91, 115–125.
- Ghurye, G., Clifford, D., 2001. Laboratory Study on the Oxidation of Arsenic III to as V. United States Environmental Protection Agency, Washington DC, p. 87.
- Gude, J.C.J., Rietveld, L.C., van Halem, D., 2016. Fate of low arsenic concentrations during full-scale aeration and rapid filtration. *Water Res.* 88, 566–574.
- Hao, O., Davis A, P., Chang P, H., 1991. Kinetics of Manganese(II) Oxidation with Chlorine.
- Hug, S.J., Leupin, O., 2003. Iron-catalyzed oxidation of arsenic(III) by oxygen and by hydrogen Peroxide: pH-dependent formation of oxidants in the Fenton reaction. *Environ. Sci. Technol.* 37 (12), 2734–2742.
- Kaegi, R., Voegelin, A., Folini, D., Hug, S.J., 2010. Effect of phosphate, silicate, and Ca on the morphology, structure and elemental composition of Fe(III)-precipitates formed in aerated Fe(II) and As(III) containing water. *Geochem. Cosmochim. Acta* 74 (20), 5798–5816.
- Kanematsu, M., Young, T., Fukushi, K., Green, P., Darby, J., 2013. Arsenic(III, V) adsorption on a goethite-based adsorbent in the presence of major co-existing ions: modeling competitive adsorption consistent with spectroscopic and molecular evidence. *Geochem. Cosmochim. Acta* 106, 404–428.
- Kelly, S.D., Hesterberg, D., Ravel, B., 2008. Analysis of soils and minerals using X-ray absorption spectroscopy. In: *Methods of Soil Analysis. Part 5. Mineralogical Methods.* SSA Book Series No.5.
- Knocke, W.R., Van Benschoten, J.E., Kearney, M.J., Soborski, A.W., Reckhow, D.A., 1991. Kinetics of manganese and iron oxidation by potassium permanganate and chlorine dioxide. *J. Am. Water Work. Assoc.* 83 (6), 80–87.
- Lan, S., Wang, X., Xiang, Q., Yin, H., Tan, W., Qiu, G., Liu, F., Zhang, J., Feng, X., 2017. Mechanisms of Mn(II) Catalytic Oxidation on Ferrihydrate Surfaces and the Formation of Manganese (Oxyhydr)oxides.
- Lanson, B., Drits, V., Feng, Q., Manceau, A., 2002. Structure of synthetic N-birnessite: evidence for a triclinic one-layer unit cell. *Am. Mineral.* 87 (11–12), 1662–1671.
- Lee, G., Song, K., Bae, J., 2011. Permanganate Oxidation of Arsenic (III): Reaction Stoichiometry and the Characterization of Solid Product.
- Manceau, A., Combes, J.M., 1988. Structure of Mn and Fe oxides and oxyhydroxides: a topological approach by EXAFS. *Phys. Chem. Miner.* 15 (3), 283–295.
- Manceau, A., Marcus, M., Grangeon, S., 2012. Determination of Mn Valence States in Mixed-Valent Manganates by XANES Spectroscopy.
- McArthur, J.M., Sikdar, P.K., Nath, B., Grassineau, N., Marshall, J.D., Banerjee, D.M., 2012. Sedimentological control on Mn, and other trace elements, in groundwater of the bengal delta. *Environ. Sci. Technol.* 46 (2), 669–676.
- Newville, M., 2001. IFEFFIT: interactive XAFS analysis and FEFF fitting. *J. Synchrotron Radiat.* 322–324.
- Nikitenko, S., Beale, A., van der Eerden, A., Jacques, S., Leynaud, O., O'Brien, M., Detollenaere, D., Kaptein, R., Weckhuysen, B., Bras, W., 2008. Implementation of a combined SAXS/WAXS/QEXAFS set-up for time-resolved in situ experiments. *J. Synchrotron Radiat.* 15, 632–640.
- Pedersen, H.D., Postma, D., Jakobsen, R., Larsen, O., 2005. Fast transformation of iron oxyhydroxides by the catalytic action of aqueous Fe(II). *Geochem. Cosmochim.*

- Acta 69 (16), 3967–3977.
- Pena, J., Kwon, K., Refson, K., Bargar, J., Sposito, G., 2010. Mechanisms of nickel sorption by a bacteriogenic birnessite. *Geochem. Cosmochim. Acta* 74 (11), 3076–3089.
- Peña, J., Bargar, J.R., Sposito, G., 2015. Copper sorption by the edge surface of synthetic birnessite nanoparticles. *Chem. Geol.* 396, 196–207.
- Perera, P.A.C.T., Sundarabharathy, T.V., Sivananthawerl, T., Kodithuwakku, S.P., Edirisinghe, U., 2016. Arsenic and cadmium contamination in water, sediments and fish is a consequence of paddy cultivation: evidence of river pollution in Sri Lanka. *Achiev. Life Sci.* 10 (2), 144–160.
- Rehr, J., Albers, R., Zabinsky, S., 1992. High-order multiple-scattering calculations of X-ray absorption fine structure. *Phys. Rev. Lett.* 3397–3400.
- Rossberg, A., Reich, T., Bernhard, G., 2003. Complexation of uranium(VI) with protocatechuic acid - application of iterative transformation factor analysis to EXAFS spectroscopy. *Anal. Bioanal. Chem.* 376 (5), 631–638.
- Scheinost, A., Rossberg, A., Vantelon, D., Xifra, I., Kretzschmar, R., Leuz, A., Funke, H., Johnson, C., 2006. Quantitative antimony speciation in shooting-range soils by EXAFS spectroscopy. *Geochem. Cosmochim. Acta* 70 (13), 3299–3312.
- Senn, A.-C., Kaegi, R., Hug, S.J., Hering, J.G., Mangold, S., Voegelin, A., 2015. Composition and structure of Fe(III)-precipitates formed by Fe(II) oxidation in water at near-neutral pH: interdependent effects of phosphate, silicate and Ca. *Geochem. Cosmochim. Acta* 162, 220–246.
- Senn, A.-C., Hug, S.J., Kaegi, R., Hering, J.G., Voegelin, A., 2017. Arsenate Coprecipitation with Fe(II) Oxidation Products and Retention or Release during Precipitate Aging. *Water Research*.
- Sorlini, S., Gialdini, F., 2010. Conventional oxidation treatments for the removal of arsenic with chlorine dioxide, hypochlorite, potassium permanganate and monochloramine. *Water Res.* 44 (19), 5653–5659.
- Sposito, G., 2008. *The Chemistry of Soils*. Oxford University Press, New York.
- Stumm, W., Morgan, J.J., 1996. *Aquatic Chemistry, Chemical Equilibria and Rates in Natural Waters*. John Wiley & Sons, Inc., New York.
- Tebo, B.M., Johnson, H.A., McCarthy, J.K., Templeton, A.S., 2005. Geomicrobiology of manganese(II) oxidation. *Trends Microbiol.* 13 (9), 421–428.
- van Beek, C.G.E.M., Hiemstra, T., Hofs, B., Bederlof, M.M., van Paassen, J.A.M., Reijnen, G.K., 2012. Homogeneous, heterogeneous and biological oxidation of iron(II) in rapid sand filtration. *J. Water Supply Res. Technol. - Aqua* 61 (1), 1–2012.
- van Beek, C.G.E.M., Dusseldorp, J., Joris, K., Huysman, K., Leijssen, H., Schoonenberg Kegel, F., de Vet, W.W.J.M., van de Wetering, S., Hofs, B., 2016. Contributions of homogeneous, heterogeneous and biological iron(II) oxidation in aeration and rapid sand filtration (RSF) in field sites. *J. Water Supply Res. Technol. - Aqua* 65 (3), 195–207.
- van Genuchten, C., Addy, S., Pena, J., Gadgil, A., 2012. Removing arsenic from synthetic groundwater with iron electrocoagulation: an Fe and as K-edge EXAFS study. *Environ. Sci. Technol.* 46 (2), 986–994.
- van Genuchten, C.M., Peña, J., 2016a. Antimonate and arsenate speciation on reactive soil minerals studied by differential pair distribution function analysis. *Chem. Geol.* 429, 1–9.
- van Genuchten, C.M., Peña, J., 2016b. Sorption selectivity of birnessite particle edges: a d-PDF analysis of Cd(II) and Pb(II) sorption by δ -MnO₂ and ferrihydrite. *Environ. Sci.: Processes Impacts* 18 (8), 1030–1041.
- van Genuchten, C., Pena, J., 2017. Mn(II) oxidation in Fenton and Fenton type systems: identification of reaction efficiency and reaction products. *Environ. Sci. Technol.* 51 (5), 2982–2991.
- van Genuchten, C.M., Gadgil, A.J., Peña, J., 2014a. Fe(III) nucleation in the presence of bivalent cations and oxyanions leads to subnanoscale 7 Å polymers. *Environ. Sci. Technol.* 48 (20), 11828–11836.
- van Genuchten, C.M., Pena, J., Amrose, S.E., Gadgil, A.J., 2014b. Structure of Fe(III) precipitates generated by the electrolytic dissolution of Fe(0) in the presence of groundwater ions. *Geochem. Cosmochim. Acta* 127, 285–304.
- van Genuchten, C., Behrends, T., Kraal, P., Stipp, S., Dideriksen, K., 2018. Controls on the formation of Fe(II,III) (hydr)oxides by Fe(0) electrolysis. *Electrochim. Acta* 286, 324–338.
- Villalobos, M., 2015. In: Feng, X., Li, W., Zhu, M., Sparks, D. (Eds.), *Advances in the Environmental Biogeochemistry of Manganese Oxides*. American Chemical Society.
- Villalobos, M., Bargar, J., Sposito, G., 2005. Mechanisms of Pb(II) sorption on a biogenic manganese oxide. *Environ. Sci. Technol.* 39 (2), 569–576.
- Voegelin, A., Kaegi, R., Frommer, J., Vantelon, D., Hug, S.J., 2010. Effect of phosphate, silicate, and Ca on Fe(III)-precipitates formed in aerated Fe(II)- and As(III)-containing water studied by X-ray absorption spectroscopy. *Geochem. Cosmochim. Acta* 74 (1), 164–186.
- Vries, D., Bertelkamp, C., Schoonenberg Kegel, F., Hofs, B., Dusseldorp, J., Bruins, J.H., de Vet, W., van den Akker, B., 2017. Iron and manganese removal: recent advances in modelling treatment efficiency by rapid sand filtration. *Water Res.* 109, 35–45.
- Webb, S., 2005. SIXPACK: a graphical user interface for XAS analysis using IFEFFIT. *Phys. Scripta* T115, 1011–1014.
- Wyckoff, R.W.G., 1963. *Crystal Structures*. Wiley.